C. ROLLER[1]
A. FRIED[2,✉]
J. WALEGA[2]
P. WEIBRING[2]
F. TITTEL[1]

Advances in hardware, system diagnostics software, and acquisition procedures for high performance airborne tunable diode laser measurements of formaldehyde

[1] Rice University Quantum Institute, Houston, Texas 77251-1892, USA
[2] Earth Observing Laboratory, NCAR, Boulder, Colorado 80301, USA

ABSTRACT A tunable diode laser absorption spectroscopy (TDLAS) instrument was deployed onboard a DC-8 aircraft as part of the International Chemical Transport Experiment – North America (INTEX-NA) during the summer of 2004 to quantify atmospheric formaldehyde (CH_2O) concentrations. A number of improvements, both software and hardware, are discussed and include the laser tuning waveform, spectral wavelength centering, and optical stabilization. In addition, the impact of perturbations to the instrument in flight is reviewed and a number of advanced TDLAS data-acquisition and processing concepts are introduced to identify the presence of optical perturbations in flight to objectively eliminate such perturbed data, assess the validity of the fitting routine in the presence of perturbed data, provide various diagnostic measures to elucidate system behavior, and assess the efficacy of various opto-mechanical improvements implemented to reduce the magnitude of such perturbations. The concepts specific to our TDLAS measurements of CH_2O should have broader and more universal applicability to measurement of other trace gases and possibly other methods of detection.

PACS 07.88.+y;42.62.Fi;82.80.Gk

1 Introduction

The technique of tunable diode laser absorption spectroscopy (TDLAS) has been widely used to measure numerous trace gases such as CO, CO_2, N_2O, CH_4, CH_2O, HCl, H_2O_2, SO_2, NO, NO_2, and HNO_3 on a variety of airborne platforms. Reviews describing such studies can be found in Schiff et al. [1], Brassington [2], Tacke et al. [3], Tittel et al. [4], and, most recently, Fried and Richter [5]. Included in this list is the trace atmospheric gas, formaldehyde (CH_2O), a gas of interest to our collective group over the past ten years. We have acquired ambient CH_2O measurements on both ground-based and airborne platforms employing TDLAS [6–11].

Formaldehyde is one of many key trace atmospheric gases that plays an important role in the photochemical production of ozone and carbon monoxide by hydrocarbon oxidation and the generation of odd hydrogen radicals HO_x ($OH + HO_2$) by

✉ Fax: 303-497-8770, E-mail: fried@ncar.edu

photolysis. In the upper troposphere such photolytic processes play a larger role in HO_x production since the main production mechanism, reactions of O (^{1}D) with H_2O, diminishes in importance as the available H_2O decreases with altitude [12]. Moreover, as many hydrocarbon oxidation reactions proceed through CH_2O as an intermediate, CH_2O becomes important in further testing our current understanding of hydrocarbon photochemistry (see Refs. [6–11] and references therein). Accurate CH_2O measurements throughout the atmosphere are thus critical to improve our understanding of atmospheric chemical processing.

Formaldehyde, which is a ubiquitous component of the lower atmosphere, is formed by the oxidation of most anthropogenic and biogenic hydrocarbons. Incomplete fossil fuel combustion, biomass burning, industrial processing, and vegetative emissions are generally considered to be the major production pathways of CH_2O over continental regions of the atmosphere. In the remote atmosphere, by contrast, methane (CH_4) oxidation becomes the dominant source of this gas (see Refs. [6–11] and references therein). Over the continents ambient CH_2O mixing ratios generally fall within the 1 to 50 parts-per-billion by volume (1 ppbv, where 1 ppbv is equivalent to an atmospheric mixing ratio of 1 part in 10^9 by volume) range, with the lower values indicative of the continental background atmosphere and the higher values indicative of polluted urban environments. In remote regions of the atmosphere mixing ratios generally fall within the range of 10 to 500 parts-per-trillion by volume (1 pptv, where 1 pptv is equivalent to an atmospheric mixing ratio of 1 part in 10^{12} by volume), and this places rather stringent demands on the instrument performance required to measure such mixing ratios. As discussed by Fried et al. [6], at typical sampling pressures and temperatures of 40–50 Torr and 303 K, respectively, an ambient CH_2O mixing ratio of 30 pptv results in an absorbance (optical density in base-e units) of 1×10^{-6} employing our typical absorption cell path length of 100 m and an absorption line at 2831.6417 cm^{-1} (integrated absorption coefficient $= 5.4 \times 10^{-20}$ cm^2 cm^{-1} molecule^{-1}). Thus, limits of detection (1σ level) for TDLAS as low as 10^{-6} for averaging times no longer than several minutes are required for studies of the clean background atmosphere on airborne platforms.

To achieve such stringent requirements our airborne TDLAS system for CH_2O has been progressively improved

over the years, and studies by Wert et al. [10, 11] and Fried et al. [8, 9] generally indicated 1σ CH_2O limits of detection (LOD) that range between 30 and 50 pptv for 1 min of averaging during airborne operation. On a few occasions, detection limits as low as 15 to 18 pptv have even been recorded by Wert et al. [11]. Although such performance is good, various perturbations during airborne operation frequently degrade our limits of detection. Optical–mechanical instabilities caused by changes in aircraft vibrations, accelerations, and cabin pressure can all negatively impact measurement performance by an order of magnitude or more. In many instances the two dominant perturbations, cabin-pressure changes and vertical accelerations, occur simultaneously as the aircraft altitude is changed.

Fried et al. [9] and Wert et al. [11] briefly discussed the impacts of aircraft cabin pressure changes on the measurement performance. However, the present paper provides further specific details regarding the concurrent changes in background structure that accompany such changes and the resulting sensitivity of the fitting approach to these perturbations employing different fitting constraints. In addition, the present paper discusses a number of advanced TDLAS data-acquisition and processing concepts to: (1) identify the presence of such perturbations in flight, allowing for corrective actions to be taken immediately; (2) identify and objectively eliminate such perturbed data after the fact where in-flight corrective actions were not successful; (3) examine the validity of the fitting routines in the presence of such optical perturbations; (4) examine the utility of various diagnostics in helping to elucidate system behavior; and (5) assess the efficacy of various opto-mechanical improvements that have been implemented to the system to minimize such perturbations in the first place. These procedures, which are a necessary first step in achieving autonomous airborne instrument operation in the future, are important for improved instrument performance, robustness, and accuracy.

The approaches discussed in this paper were applied to our TDLAS measurements of CH_2O acquired onboard the NASA DC-8 aircraft during the Intercontinental Chemical Transport Experiment – North America (INTEX-NA) study in the summer of 2004. Airborne CH_2O measurements were acquired over 17 flight missions, covering large regions over the continental United States, Canada, and the North Atlantic Ocean. Aircraft altitudes spanned the range from several hundred meters to 12 km. Although the concepts are specific toward our TDLAS measurements of CH_2O, they should have broader and more universal applicability for other trace gases, and perhaps even other methods of detection.

2 TDLAS system deployed on INTEX-NA 2004 and acquisition procedures

2.1 TDLAS system and inlet

The current TDLAS aircraft system has been described in detail by Fried et al. [9] and Wert et al. [11] and the technical details are briefly discussed here. A schematic diagram is shown in Fig. 1. The infrared radiation (3.5 μm) from a liquid-nitrogen-cooled lead-salt diode laser is directed through a multipass astigmatic Herriott absorption cell (Aerodyne Incorporated, 100-m optical path length and 3-l volume) using a series of off-axis and flat mirrors. The cell output beam ($\sim$ 12 to 30 μW) is imaged onto cryogenically cooled InSb sample and reference detectors, as shown. The reference detector arm contains a reference cell with pure CH_2O at 10-Torr, which is used for wavelength locking (to be discussed).

The laser is repetitively tuned across a CH_2O absorption feature at 2831.6417 cm^{-1} by sweeping the injection current using a function-generator card and a triangle waveform at 25 Hz, which produces two scans ('up' and 'down' scans) for each triangle waveform. An additional triangle waveform rapidly modulates the laser at 50 kHz. The detector signals are directed into lock-in amplifiers where the $2f$ (100 kHz) demodulated signals from both channels are determined. The outputs of the lock-in amplifiers are further co-averaged employing a 16-bit analog-to-digital converter
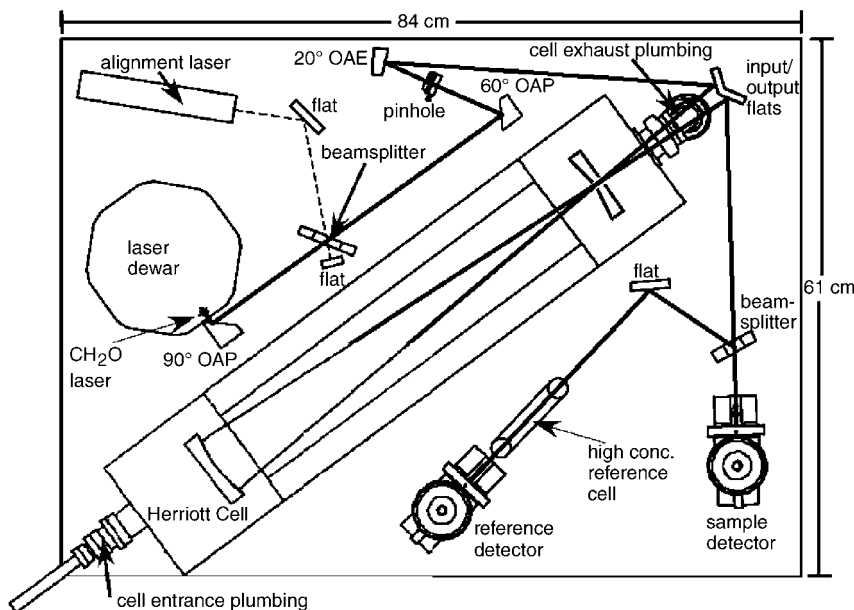

FIGURE 1 Schematic of the laser and optical system housed in a temperature-stabilized enclosure. The enclosure dimensions are approximately 33$''$ long $\times$ 24$''$ wide $\times$ 12$''$ high. OAP – off-axis-parabolic; OAE – off-axis-ellipsoidal. ©Copyright 2003 – American Geophysical Union. Reproduced by permission of American Geophysical Union [11]

data-acquisition card and a computer. The data-acquisition card samples at a frequency of 10 kHz (400 points per period of the sweep waveform) and is triggered with a TTL signal from the function-generator card.

Ambient air is continuously drawn through the Herriott cell at typical flow rates of 8–10 standard liters per minute (slm, where standard conditions are defined as $T = 273.15$ K and $P = 760$ Torr) employing a 1.3 cm outer diameter PFA Teflon line mounted in a heated winglet structure [9]. The winglet protruded outside the aircraft boundary layer and faced perpendicular to the aircraft flow. The inlet line was heated in the winglet structure to 35 °C to within a cm of the inlet entrance. An oil-free scroll pump was used to generate the flow through the gas cell and inlet. An inlet-pressure controller, which employs a standard capacitance manometer pressure transducer mounted on the cell, was used to control the cell pressure at around 50 Torr. Zero air (ambient air with CH_2O scrubbed out) generated with a commercial scrubber (manufacturer: Advanced Analytical Device Company) and calibration standards are directed into the inlet near the tip using separate addition ports. During zero-air addition, the scrubbed airflow was switched into the inlet at a flow rate of a few slm higher than the cell flow.

During calibration, CH_2O standards from permeation devices were introduced into the inlet downstream of the zero-air flow using a separate calibration addition port (see Ref. [9] and references therein). Calibration spectra are typically collected at CH_2O concentrations of ~ 13 to 14 ppbv, which produces $2f$ absorption signals with high signal-to-noise ratios. The calibration spectra are stored digitally in computer memory for regression fitting for the determination of sample gas mixing ratios, as will be further discussed.

2.2   *Data acquisition, optical perturbations, and temperature stability*

The term 'optical noise', as used in this paper, refers collectively to all changes in background structure, and this includes unwanted periodic etalon fringes and less well defined background structural changes due to small changes in beam alignment, both internal and external to the multipass sampling cell. At the very least, such subtle alignment changes can dramatically affect retrieved concentrations whenever the time evolution of the true background structure does not match the captured background structure acquired during zero-air addition (to be discussed). Such alignment changes can also introduce more insidious effects from scattering, which can result in multiple beams impinging upon the detector. The result is an undulating background structure comprising many frequencies, amplitudes, and time constants from multiple scattering sources.

As in past studies we have employed the technique of rapid background subtraction to significantly reduce the effects of such optical noise structure (see for example Refs. [6, 11]). Spectral background structure is captured using this approach by rapidly measuring zero air just prior to and immediately after acquiring ambient sample spectra. Over the years we have employed slightly different variations in the acquisition of background and calibration/ambient spectra. During INTEX-NA, background spectra were typically acquired for

either 10 or 15 s and this was followed by a 30- or 60-s ambient acquisition period or a 30-s calibration acquisition. A second background acquisition period then followed. Between each acquisition switch, the sample cell was flushed with the new sample for ~ 5 s before data acquisition was initiated. Each ambient spectral block was repeated approximately every 55 to 85 s and was accompanied by two acquired background spectra, one collected before (pre-background) and one after (post-background) and two flush periods. For facility of discussion, we hereafter refer to each ambient spectral block as a '1-min average' regardless of the specific sequence employed. Subtraction of the pre- and post-backgrounds neighboring the ambient sample spectra was performed using a linear time weighted subtraction (LWS) scheme. In this procedure the background spectra were averaged using weights linearly proportional to the time in the acquisition sequence. The resulting LWS background spectrum was subtracted point by point over the 200 scan channels from the intervening ambient spectra. The ambient sample spectra in all cases were acquired in 1-s intervals, each consisting of 25 averaged spectra for the up and down ramps of the triangle sweep waveform (to be further discussed). Obviously, 1-s ambient spectra acquired at the start and end of the ambient sequence are most affected by the pre-background and post-backgrounds, respectively.

If the background structure is stable or changes in a smooth linear fashion in time, the background structure is faithfully removed with this LWS procedure. However, in the present airborne system shown in Fig. 1, a number of optical components can cause subtle alignment changes as the cabin pressure is changed and/or the airplane experiences vertical accelerations, with the consequence that the above LWS becomes less valid. Throughout the rest of this paper we refer to such time periods as 'perturbed'. The two largest offending components are the Herriott cell and its input window. As discussed by Dyroff et al. [13], dynamic flexure of the Herriott cell end plates and base plate occurs as the pressure differential across the cell changes with cabin pressure, and this causes slight misalignment of the cell mirrors. In addition, as the cell window is sealed using a flexible O-ring, the window can move with changing differential pressure. Finally, a number of other components such as the cell input/output flat mirrors and potentially the laser position in the liquid-nitrogen dewar as well as the dewar position can also change due to vertical accelerations.

It is important to emphasize that the perturbations just discussed are shared by many if not most TDLAS systems, and that the magnitude of such perturbations in the present system is small; during the INTEX-NA study the equivalent line center absorbance magnitude of such perturbations was typically around 10^{-5} for 1-s averages. Despite this fact, such optical noise, which may be negligible for highly polluted conditions (tens of ppbv of CH_2O), is not compatible for measurements of background CH_2O levels in the sub-ppbv range. The latter requires at least one order of magnitude lower optical noise.

Another important consideration for highly sensitive airborne measurements of CH_2O is temperature stability. It is well known that temperature stabilizing the entire optical system is essential in minimizing small thermo-mechanical movements of the optical components and serves to stabilize the spectral background structure over time periods of sev-

eral minutes. This becomes important when operating on an aircraft where cabin temperatures can dramatically change by as much as $15\,°C$ over the duration of an 8–10-h flight, depending upon location on the aircraft and the particular aircraft. To address this problem, we have successfully flown a temperature-stabilized optical enclosure system over the past five years [11]; during a typical 7–8-h INTEX-NA flight, the air temperature at the center of our thermally controlled optical enclosure was typically maintained at $30.4 \pm 0.2\,°C$ (maximum deviation of $0.7\,°C$), and this compares to a cabin temperature of $26.5 \pm 1.8\,°C$ (maximum deviation of $7.1\,°C$). Since not every TDLAS system incorporates such measures, it is instructive to explicitly show the optical perturbations that may arise from such cabin-temperature perturbations. This is illustrated by the Allan variance plots of Fig. 2.

The Allan variance concept was first introduced by Allan in 1966 for characterization of frequency standards. However, Werle et al. [14] first popularized its use for assessing the stability of diode laser optical systems. An Allan plot is constructed by repetitively sampling a constant input mixing ratio in very small time increments (of 1 s or less), and the resulting average measurement variance between adjacent groups of data is displayed on a log–log plot as the number of elements in each group is successively increased (i.e. increasing the integration time). The measurement variance decreases linearly with integration time (white-noise regime) until an optimum integration time, t_{opt}, is reached, whereupon instrument drifts start to dominate. Throughout this study Allan variance measurements are employed as one tool in assessing background stability, and more generally overall instrument stability, as a function of different operational parameters.

Figure 2 shows successive Allan variance plots acquired at various time intervals after switching on our optical enclosure temperature stabilizing system. The temperature changed from ambient laboratory conditions of $\sim 23\,°C$ to the set point of $30\,°C$ (the alignment temperature), very similar to the cabin-temperature excursions encountered during INTEX-NA. All of the profiles except the $30\,°C$ profile were acquired

under conditions of changing temperature; the $30\,°C$ profile was at stable temperature conditions. The measurements here were acquired using background zero air. As the enclosure temperature begins to stabilize at $30\,°C$ after ~ 73 min, the precisions as indicated by the Allan variance and stability times greatly improve. After stabilization, the minimum in the Allan variance extends over ~ 30 s and indicates a 1σ CH_2O LOD of 28 pptv. Choosing a mid temperature of $27\,°C$ where the temperature is still changing degrades the stability time to ~ 10 s and the ultimate detection limit by a factor of 2.5. While the temperature-induced optical perturbations of Fig. 2 may be somewhat extreme because the heating rates are a factor of ~ 2 higher than that actually encountered in flight during INTEX-NA, the total temperature swings between the laboratory tests and the aircraft environment are very similar. This, coupled with the fact that more extreme rates of temperature change are likely on other aircraft platforms, graphically illustrates the importance of active optical temperature control for high performance on airborne platforms. Although we have not characterized the dependence of the temperature-induced optical perturbations on heating rates, it is logical to assume that higher heating rates should produce higher perturbations at any given time.

2.3   *Triangle waveform for TDLAS wavelength tuning*

As discussed previously, a triangle waveform was used to repetitively sweep the laser at a rate of 25 Hz across the CH_2O line of interest. In the past we employed a sawtooth [15] waveform for this purpose, and this was later modified using a hyperbolic cotangent function on the descending portion of the waveform to reduce discontinuities at the turning points. Figure 3 illustrates examples of both types of scanning waveforms. When using the modified sawtooth waveform, we always encountered severe perturbations at the start of each scan ramp due to laser 'fly back' as the laser is abruptly tuned backwards over the absorption region of interest. This frequently results in a 'ringing-like' feature at the start of each ramp, which perturbs approximately the first 30 scan channels and in many instances produces a low-frequency undulation over the entire ramp. In the best of circumstances such perturbations reduce the available number of scan channels that can be utilized during fitting. In many cases the entire scan is affected, and this results in added noise to the retrieved fit mixing ratios. The triangle waveform by contrast has less severe tuning transitions because the laser injection current is swept with equal but opposite tuning current rates. In this way nearly the entire number of scan channels can be utilized and this type of waveform produces two effective absorption scans over the region of interest during one scan cycle. Wienhold et al. [16] have successfully employed this type of waveform in their airborne spectrometer. However, these researchers observed a hysteresis in the laser tuning between the 'up' and 'down' ramps of the triangle waveform and this required the data from each ramp to be aligned before co-addition. We observe a similar tuning hysteresis but treat the data slightly differently. During INTEX-NA, the 'up' and 'down' ramps were treated as independent samples using their own respective calibration and background
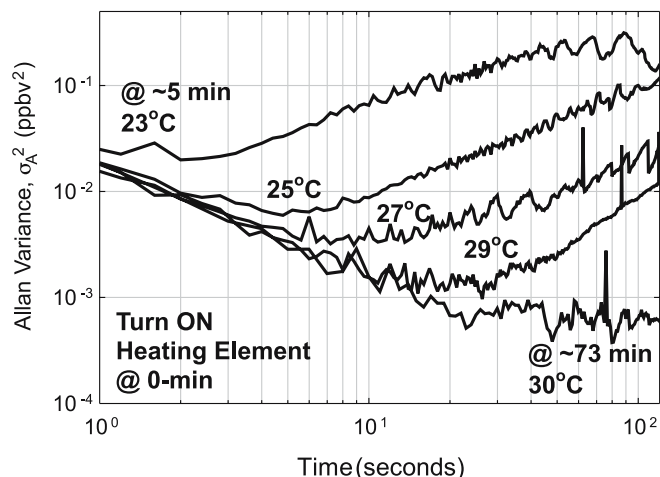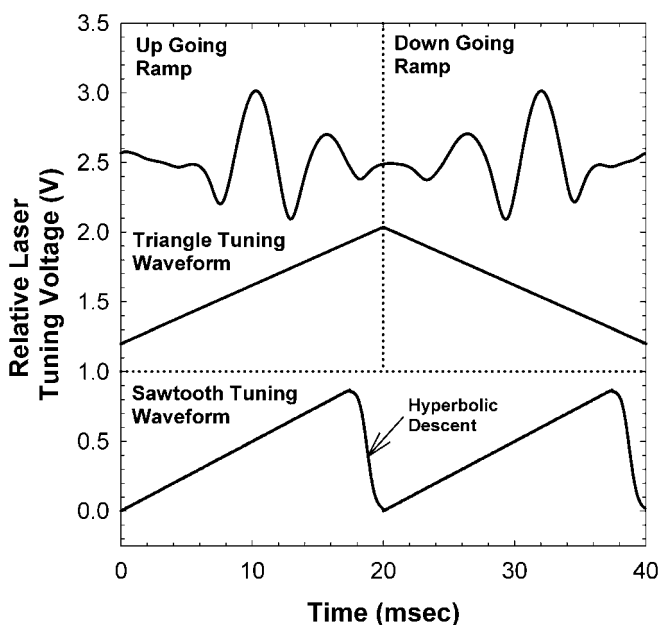
FIGURE 2   Allan variance plots of measured 10-min CH_2O concentration trends comprising 0.5-s integrated data points taken at successive time intervals (5, 19, 32, 46, and 73 min) after switching on the optical enclosure heating system. As can been seen, 1 h of temperature stabilization is required to ensure adequate stability of the optical background structure

FIGURE 3 The *upper plot* shows a triangle tuning waveform (25 Hz) and the corresponding retrieved $2f$ CH$_2$O spectra. The *lower plot* is an example of a sawtooth waveform (50 Hz) with hyperbolic cotangent descent

FIGURE 4 Reciprocal of tuning rates in channel numbers per free spectral range (FSR) of the Ge etalon, where FSR = 0.01601 cm^{-1}, for the sawtooth waveform with hyperbolic descent (▲ symbol), up portion of triangle ramp (● symbol), and down portion of triangle ramp (■ symbol). The tuning range is slightly different for the two different types of scan ramps since different amplitudes were applied

FIGURE 5 Probability density functions (PDFs) for 2750 1-s concentration measurements of zero air for C_{up} and C_{down} as well as the average of the two concentration values. The resulting improvement in the standard deviation, 1σ, for the averaged CH$_2$O concentration trend is a factor of $\sim \sqrt{2}$ and is the expected improvement if the noise is sufficiently random and uncorrelated

spectra in the fitting procedures to generate a concentration (C_{up} and C_{down}) every 1 s for each ramp. These results are then combined to produce one averaged concentration value every second.

A germanium (Ge) etalon crystal of 7.62-cm length and free spectral range (FSR) of 0.01601 cm^{-1}/period (at 2831.6 cm^{-1}) was used to determine the wavelength-tuning characteristics of the laser for triangle and sawtooth waveforms. The reciprocal of the tuning rates in terms of channel numbers per etalon FSR period for the sawtooth waveform with hyperbolic descent and both the up- and down-going ramps of the triangle waveform are shown in Fig. 4. The tuning range is slightly different for the two different types of scan ramps since different amplitudes were applied. Nevertheless, as can be seen the non-linear portion of the tuning curve for the modified sawtooth ramp extends over a larger portion of the scan ($\sim 33\%$) than that for the triangle ramp (~ 15 to 20%), and this has a direct bearing on the useful number of scan channels that can be employed in the fit. It is interesting to note that the curvature at the end of the down ramp is considerably less than that at the start of the up ramp, and the reasons for this need to be further investigated. Because of the different tuning rates random and uncorrelated noise on the up and down ramps (whether electronic or optical noise) will often result in an averaged fit value whose uncertainty is reduced by a factor of $\sqrt{2}$, and this is shown by the probability density function (PDF) of Fig. 5.

The PDF is a histogram representation used throughout this paper to describe data sets and relevant statistical measures. For a random variable this corresponds to a Gaussian distribution. In particular, the relative heights and widths of the PDF for a given variable under consideration are used to assess comparative system performance under various operating conditions. The PDF becomes higher and narrower for a particular variable for certain acquisition conditions, and
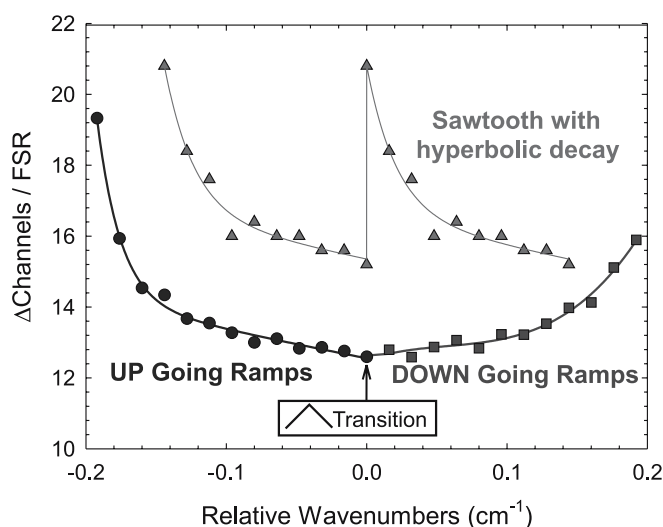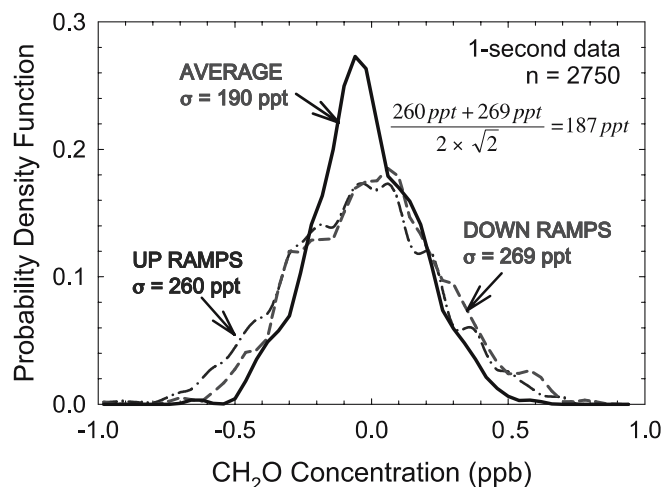
this reduced distribution spread along with a reduced value for the distribution mode indicates an improvement in system performance.

In Fig. 5 we plot the PDF of the retrieved CH$_2$O concentrations acquired using zero air for 2750 1-s measurements for both the up and down ramps. The PDFs are estimated from histograms of the C_{up} and C_{down} time series. Also shown in Fig. 5 is the PDF for a time series obtained from averaging respective C_{up} and C_{down} points, and indeed there is an associated reduction in the uncertainty of $\sim \sqrt{2}$ (1σ) suggesting that the noise between C_{up} and C_{down} is sufficiently random and uncorrelated. In many but not all cases we observe such a $\sqrt{2}$ improvement. However, in the presence of systematic perturbations to the optical system, such as low-frequency background curvature, both C_{up} and C_{down} can be affected

differently, in which case a $\sqrt{2}$ improvement in the 1σ uncertainty will not be achieved.

2.4   *Cross correlation for laser scan stabilization and indicator of scan perturbations*

The reference arm of the optical train, comprising the reference cell and detector shown in Fig. 1, provides strong unambiguous high signal-to-noise $2f$ CH_2O absorption spectra that can be used in real time to correct for laser wavelength drifts between scans before co-averaging. Laser wavelength drifts can occur from a multitude of causes, including laser substrate temperature instabilities, instabilities of the laser current/temperature controller arising from changes in its surrounding ambient temperature, and changes in the liquid nitrogen boil off temperature due to changes in pressure over the liquid nitrogen. Werle et al. [14] demonstrated the requirement for co-aligning spectral scans before co-averaging in order to avoid deleterious effects of such laser wavelength drifts during sweep integration. A number of strategies have been successfully employed by various research groups for this purpose, involving either the application of a feedback signal to the laser temperature or current controllers or the shifting of acquired spectra in memory before co-averaging. Our airborne system incorporates a combination of both strategies: we utilize fast shifting in memory employing the absorption line center to co-align each scan before co-averaging and the application of feedback current to the laser controller at the end of each background–ambient–background acquisition sequence to keep the absorption feature centered in the scan window.

Various spectral centering routines have been utilized to co-align spectra stored in memory using acquired reference spectra. The most straightforward approach is to line up the maximum-peak points of the $2f$ reference spectra, but this approach is limited in that it only takes into account one point, which may be affected by optical or electronic noise and gives rise to large uncertainties in the determined spectral line center. Employing the zero crossing of the first harmonic of the reference signal can be affected by small dc drifts in the $1f$ signal, which can add noise to the centering routine. A more complex approach looks not only at the peak of the $2f$ absorption signal, but also at the two negative lobes, which are averaged and used in conjunction with the peak to determine the line center. We have in the past employed a variant of this three-point approach, which utilized equal-intensity $2f$ absorption points on both sides of the absorption peak to identify the position of the line center. Although this procedure worked reasonably well, large asymmetries due to large optical fringes and/or time-dependent perturbations across a scan can add additional uncertainty in locating the line center.

May [17] successfully utilized the autocorrelation function for spectral scan stabilization to correct for laser wavelength drifts every 30 s. This approach was used to determine both the sign and amplitude of the laser wavelength drifts, which in turn allowed appropriate laser scan adjustments to be applied to keep the spectral scan centered within the fit window. The advantage of the autocorrelation is that all points across the reference spectrum are analyzed to determine the line center position, resulting in a more accurate determin-

ation of the desired laser wavelength shift than just analyzing one or three points. In addition, the use of an autocorrelation routine provides three other significant advantages not previously addressed: (1) it identifies time periods when the signal amplitude from the sample arm may have significantly changed due to changes in the optical alignment up to and through the Herriott cell (the reference calibration arm shares most of the same optical components as the signal arm) as well as malfunctions in the scan board, etc.; (2) it is less susceptible to large amplitude changes in the reference arm due to optical misalignments; and (3) it readily identifies changes in laser tuning rate and laser power during the time between calibration and ambient acquisition due to persistent systematic laser wavelength drifts and the attendant correction signals that are applied. For example, we have experienced large changes in laser tuning rates due to scan-board malfunctions caused in part by excessive computer heating. Whatever the cause, changes in laser tuning rate between calibration and ambient acquisition can result in systematic fitting errors.

In recognition of these advantages, our INTEX-NA system incorporates an autocorrelation routine for: (1) memory spectral co-aligning on a scan-by-scan basis prior to co-averaging; (2) subsequent active current feedback to the laser controller at the end of each acquisition cycle; and (3) the identification of time periods when a new calibration spectrum should be acquired arising from the various perturbations discussed above. For the INTEX-NA mission, a reduction in the peak magnitude of the autocorrelation of 10% was used to indicate the need for a new calibration spectrum.
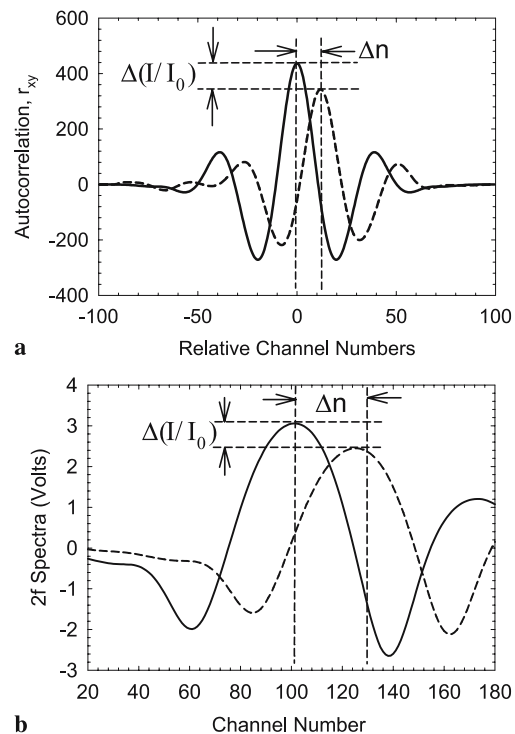

FIGURE 6 (**a**) The autocorrelation of the reference taken at the time of calibration (*solid line*) and after a wavelength drift (*dashed line*) and reduction in magnitude. (**b**) Respective $2f$ signal traces in the reference arm. Indicated in the autocorrelation is the reduction in power ($\Delta I/I_o$) and wavelength shift in terms of channel numbers (Δn)

The autocorrelation, R_{xy}, is computed using (1):

$$R_{xy}(t) = x(t) \otimes y(t) = \int_{-\infty}^{+\infty} x(\tau) y(t + \tau) \, d\tau . \qquad (1)$$

Here $x(t)$ and $y(t)$ are the reference-arm spectra acquired during calibration and during subsequent ambient measurements, respectively. Figure 6a and b show the reference-arm autocorrelation and second-harmonic spectra taken at the time of calibration and after a wavelength drift and associated power change.

To demonstrate the robustness of the autocorrelation algorithm for stabilizing and centering spectra, the laser beam was periodically and rapidly perturbed in its amplitude using a tuning-fork optical chopper placed in the beam path. This simulates rapid amplitude changes across each scan ramp due to severe aircraft vibrations and an associated movement in optical alignment while maintaining a stable absorption line center position. Such perturbations can occur when flying in a turbulent boundary layer. Samples of several chopper-perturbed CH_2O reference spectra are shown in Fig. 7a. Figure 7b shows the resulting determination of the $2f$ absorption line center using our previous three-point approach and the autocorrelation under such perturbed operating conditions. As can be seen, the three-point approach produced significantly larger channel-number swings than the autocorrelation technique by on average a factor of 3.4.
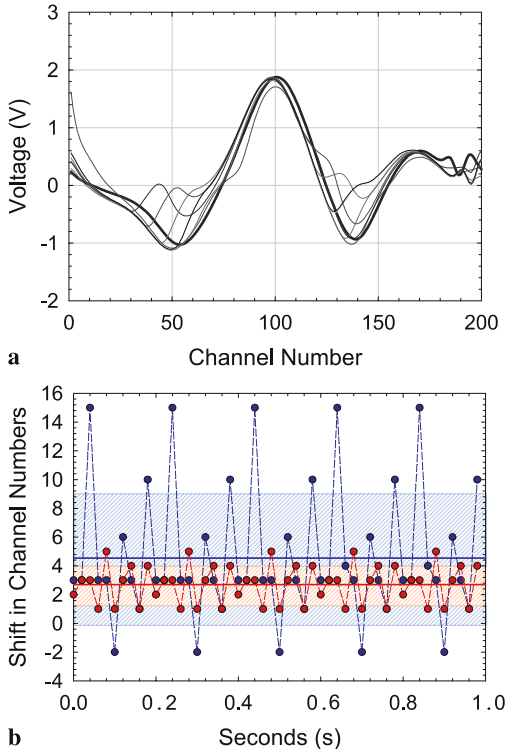

a

b

FIGURE 7 (**a**) Measured sample CH_2O spectra perturbed with a tuning-fork optical chopper. (**b**) Determined memory shift in channel numbers based on line center identification using the autocorrelation centering routine (*red*) and a three-point centering routine (*blue*). The autocorrelation results in more accurate and more stable absorption line center identification by a factor of ∼ 3.4 compared to the three-point centering approach

2.5 *Least-squares fitting employed in CH_2O concentration determinations*

Ambient CH_2O concentrations are determined by fitting the calibration spectrum of known concentration to the sample spectra of unknown concentrations using a multiple linear regression approach employing singular value decomposition (SVD). The original implementation of this technique in our TDLAS measurements has been described by Sewell et al. [18], and the veracity of the retrieved CH_2O concentrations has been repeatedly verified over the years. However, we further examine here two aspects of this fitting approach that have not been explicitly discussed: (1) the dependence of the retrieved concentrations on the terms employed in fitting the background in the presence of large optical perturbations and (2) the optimum fit window during such perturbations.

Using the reference spectra and the procedures previously discussed, the sample spectra line centers are co-aligned with the calibration spectrum. The linear-least-squares fit is performed on both the 'up' and 'down' scan ramps independently using a selected fit window to accommodate the absorption feature with sufficient spectral background on both sides for each scan ramp. To accommodate residual background structure after background subtraction, three background terms (offset, linear, and quadratic) are added as basis functions to the regression fit [18–20]. These terms respectively account for a dc offset, a linear slope, and quadratically-curved background structure between sample and calibration spectra. During perfect background subtraction these three terms should all be close to zero. Equation (2) shows a linear combination of the above three background functions plus an additional term for the calibration spectrum used to describe and fit each ambient spectrum:

$$amb = (A_1 \, cal) + (A_2) + (A_3 X) + (A_4 X^2) . \qquad (2)$$

Here cal is the calibration spectrum, the A's are the coefficients that are determined in the fit, amb is the measured sample spectrum of unknown concentration, and X represents the channel numbers across the scan.

Singular value decomposition is used to minimize the least-squares residuals in the over-determined system (more data points than parameters) to estimate the fit coefficients by minimizing the χ^2 function defined in (3) [21]:

$$\chi^2 = \sum_{i=1}^{N} \left[amb_i - \left(A_1 cal_i + A_2 + A_3 X + A_4 X^2 \right) \right]^2 . \qquad (3)$$

The fit is carried out over the N channels defined by the fit window. The unknown ambient concentration is then determined by multiplying the retrieved A_1 coefficient by the concentration of the CH_2O standard used to generate the calibration spectrum. The fit residual, to be discussed later, is defined as the absolute average difference of the fit spectrum determined by the coefficients and the measured sample spectrum.

We now examine the dependence of the retrieved fit concentrations on the terms employed in fitting the background and the size of the fit window during time periods where large optical perturbations were present. In all cases the 'up'

and 'down' averages are used. Since each daily flight was characterized by numerous vertical profiles with large attendant cabin-pressure changes, one can find time periods from any of the flights throughout the INTEX study for these examinations. Flight 13 on July 28th, 2004, however, is particularly advantageous for this purpose because it contains long time periods with vastly different optical behavior. This flight occurred before additional measures were fully implemented to mechanically stabilize the system. Aircraft altitude changes are necessarily accompanied by other aircraft changes; namely, changes in pitch, accelerations, airspeed . . . . Aircraft cabin pressure was continuously recorded throughout the INTEX-NA mission by a small capacitance monitor mounted on our TDLAS. The results for flight 13 are shown in Fig. 8. Here the retrieved fitted CH_2O concentrations for combined 'up' and 'down' ramps for each 1-s measurement are displayed along with the cabin pressure and aircraft altitude. As is immediately obvious, this figure consists of three stability regions: (1) a 'stable region' comprising ~ 1.5 h of constant-altitude flying with constant cabin pressure, constant aircraft speed, and constant aircraft pitch; (2) an 'intermediate region' comprising ~ 30 min of intermediate cabin-pressure changes; and (3) a 'perturbed region' comprising ~ 2 h with large perturbations in cabin pressure and, starting at $\sim 15:25$ and extending throughout the rest of this period, large continuous changes in both aircraft speed and pitch, necessitated by flying in formation with a much slower aircraft during measurement intercomparisons. It is important to point out that all measurement periods in Fig. 8 were carried out over the remote Atlantic Ocean far removed from local pollution sources, as further evidenced by low values for anthropogenic tracers such as carbon monoxide, ethane, and benzene. Hence, we can immediately rule out the possibility that the increased measurement scatter in the retrieved CH_2O concentrations

during the 'intermediate' and 'perturbed' regions was caused by large ambient variability.

As can be seen, even small cabin-pressure changes of ~ 7 Torr in the 'intermediate region' caused significant optical perturbations and changes in the retrieved 1-s fit concentrations by as much as 1.6 ppbv. During the 'perturbed region' the cabin-pressure changes were much larger, resulting in even larger swings in the retrieved CH_2O concentrations. During these time periods there are frequent breaks in the retrieved data due the necessity of stopping the acquisition to carry out small alignment changes. Even after these were accomplished, the overall standard deviation for the 'perturbed region' is still a factor of ~ 3 higher than the 'stable region'. As will be shown, this significantly larger variability signifies a breakdown in the validity of the background LWS and this is further reflected by the fact that acquired backgrounds alternately under-predict and over-predict the true backgrounds underlying each 1-s data point. Figure 9 depicts one example of the structure of the pre- and post-backgrounds acquired during the 'stable' and 'perturbed' regions. As indicated, the entire background shape has changed during the latter period. Additional plots will be presented showing how other variables are likewise affected by such optical perturbations.

Figure 10 shows the PDF of the replicate precisions (σ_r) of 1-s data for both the 'stable' and 'perturbed' regions of flight 13 using only the offset background fit term (A_2) compared to that using the higher-order background terms (offset, linear, and quadratic). Over each '1-min average' a measurement standard deviation is calculated, and Fig. 10 plots the distribution of these standard deviations for the cases considered. This procedure reduces the effects of ambient CH_2O concentration variability since it examines the variability about each 1-min retrieved result. The modes of the resulting distributions thus represent a measure of the 1-s instrument limits of detec-
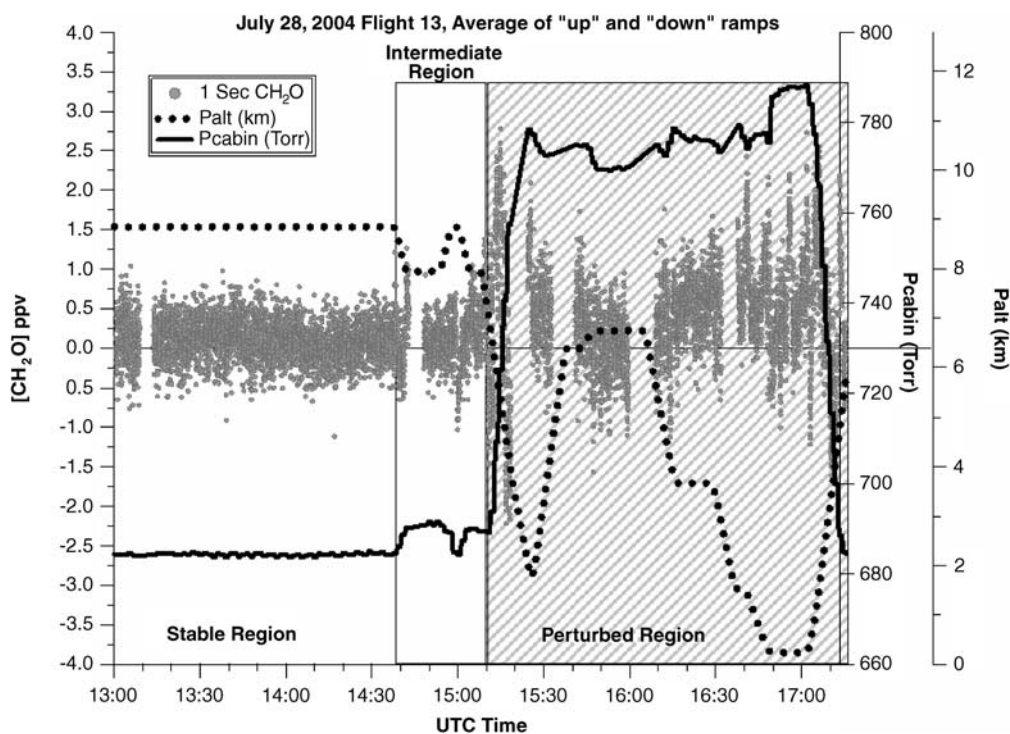

FIGURE 8 Plot of INTEX-NA 1-s CH_2O concentration data measured on July 28th, 2004. The region on the *left* is relatively stable as compared to the 'perturbed' region on the *right-hand side* of the plot due to large changes in cabin pressure. P_{alt} – aircraft altitude, P_{cabin} – aircraft cabin pressure
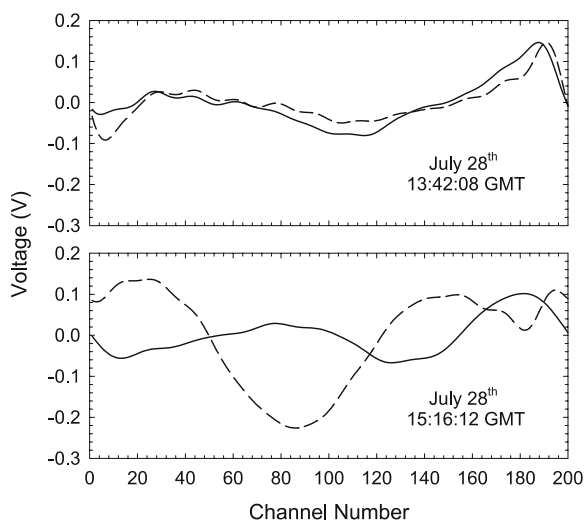
FIGURE 9 (*Top plot*) Pre- and post-background spectra acquired during the stable region depicted in the plot of Fig. 8. The background amplitude residual (BAR) value for this plot, computed by subtracting the pre- and post-backgrounds point by point over the fit window and computing the average absolute residual value in terms of concentration units (see text for discussion of this parameter), is 0.16 ppbv. (*Bottom plot*) Pre- and post-background spectra acquired during the perturbed region depicted in the plot of Fig. 8. The BAR value for this plot is 1.32 ppbv
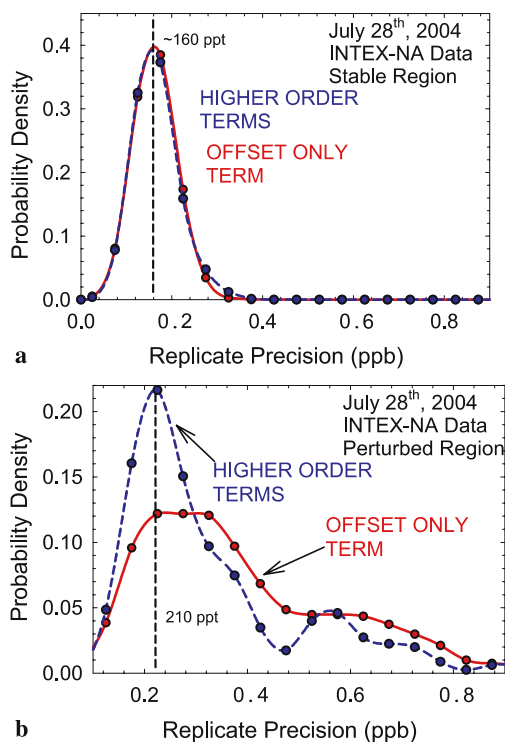

FIGURE 10 PDF plots of replicate precisions using only an offset or higher-order (offset, linear, and quadratic) background basis terms in the fit over (**a**) the stable region and (**b**) the perturbed region shown in Fig. 8. The replicate precisions were determined from the measurement standard deviations of 60 1-s data points acquired during numerous ambient acquisition cycles. The modes of the distributions are shown

tion for the conditions considered during airborne operation. As can be seen, during the 'stable region' one cannot distinguish any difference in the quality of the fit whether one uses a simple offset background basis vector or an offset coupled with linear and quadratic terms (higher-order terms). During

the 'perturbed region', the distributions are significantly less Gaussian, exhibiting in both cases long tails out to higher-precision estimates and the appearance of a secondary mode. However, the use of the higher-order background terms in these cases improves the quality of the fit. These higher-order terms accommodate residual background structural changes over the measurement cycle significantly better than the fits with only the offset term; in addition to a less normal-like distribution the latter exhibits a less distinctive primary mode. In the future more sophisticated background basis terms using the residuals of the fit backgrounds will be employed as a corrective term to the background basis vectors.

Figure 11 further examines the 1-s replicate precisions (using the higher-order background terms) as a function of the size of the fit window. This figure shows the replicate precision PDFs over the 'stable' and 'perturbed' regions of July 28th for two different spectral fitting windows: channels 40 to
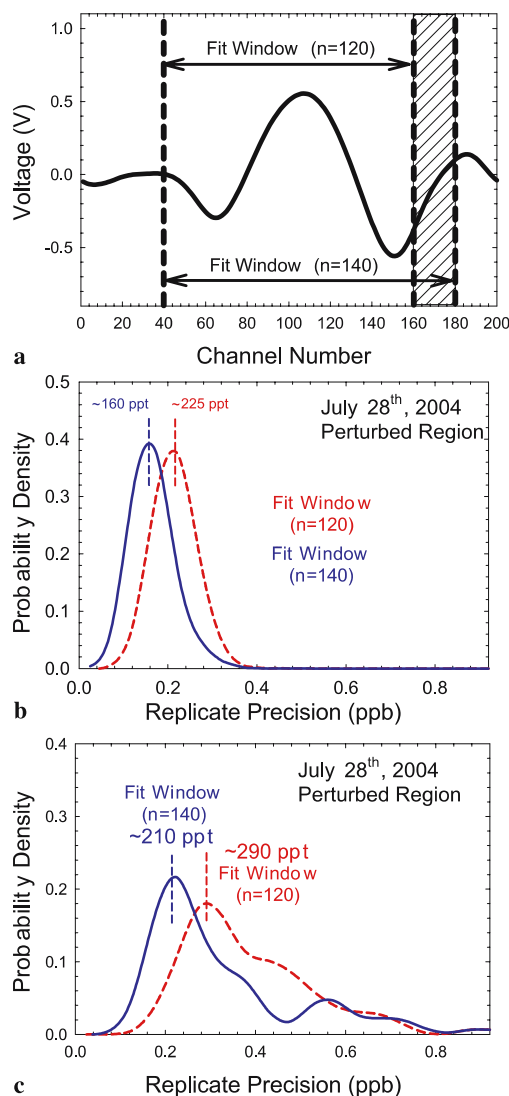

FIGURE 11 (**a**) Two spectral fitting window sizes of 120 and 140 channel numbers, which represent the portion of the spectrum used in the fitting routine. The spectrum shown is a 13.6 ppbv calibration acquisition. (**b**) PDF plots of the replicate precisions retrieved for the 120-point (*dashed red line*) and 140-point (*solid blue line*) window sizes for the stable region and (**c**) for the perturbed region of Fig. 8

160 ($N = 120$) and channels 40 to 180 ($N = 140$). Figure 11a depicts these two windows, while Fig. 11b and c show the resulting PDFs for the two stability regions. As can be seen, a small increase of only 20 channels in the fit window improves the mode of the fit distributions by $\sim 28\%$ for both the 'stable region' and the 'perturbed region'.

Despite the above improvements in the fits employing the higher-order background terms and the wider fitting windows, these procedures still do not eliminate the effects of large optical perturbations caused by changes in aircraft: cabin pressure, pitch, and accelerations. As can be seen in Figs. 10 and 11, the distributions are significantly more Gaussian in the 'stable region' compared to the 'perturbed region'. The above aircraft perturbations not only affect retrieved CH_2O concentration determinations but also a number of other parameters, as will now be discussed.

3   TDLAS performance assessment during the airborne INTEX-NA study

3.1   *Parameters used in the identification of optically perturbed time periods*

Although the large swings in the retrieved CH_2O concentrations of Fig. 8 were very useful as a first step in identifying optically perturbed time periods, other measures must also be employed. This is particularly pertinent when carrying out altitude profiles over continental regions where one can readily encounter large ambient CH_2O variability. Simply eliminating regions of high concentration variability may erroneously eliminate true ambient data in such cases. We have identified a number of other diagnostics that can readily be used to identify optically perturbed time periods and hence a breakdown in the validity of our LWS assumption for the backgrounds as well as the validity of the fitting procedure using the offset, linear, and quadratic basis terms. These diagnostics are background amplitude residuals (BAR), pre- and post-background subtraction concentration differences ($\Delta C = |C_{B1} - C_{B2}|$), fitted background absolute areas (FBAA), fit residuals, and average channel standard deviations (σ_{ch}). Each of these diagnostics provides unique information and this will be examined below.

In each case, with the exception of ΔC, the diagnostics are measured in voltage units. To account for differing laser output powers throughout the day and to enable meaningful comparisons with data collected on different days, these values are converted to 'relative concentration' units by taking the quotient of the appropriate signal with a calibration factor (the peak of the calibration spectrum signal normalized by the calibration concentration). Such relative concentration values (or concentration-channel number area values in the case of the FBAA) are only diagnostics and by no means are meant to convey the actual precision with which a measurement can be made. Only the replicate precisions can be used in this capacity. Instead, the aforementioned diagnostics serve as general indicators of instrument performance and the presence of optical perturbations. In addition, in the case of the BAR and average channel standard deviation diagnostics, no fitting is involved and thus the results may contain noise components that are not present by our fitting to a calibration spectrum. Hence, the most appropriate way to use the various diagnostics is to compare the retrieved values of each diagnostic with itself under different conditions, and not with one another.

As previously discussed, Fig. 9 shows one of many examples we encountered for successive backgrounds (pre- and post-backgrounds) surrounding '1-min' ambient acquisition periods during 'stable' and 'perturbed' optical regions. Such plots are displayed in real time during acquisition to give the operator one measure of system performance. Although such data does not give information about the time evolution of optical perturbations and whether the LWS is still valid, the persistence of large structural background changes, as in the bottom panel of Fig. 9, is taken as one indication for the need to stop data acquisition to carry out optical realignment. In addition, we tabulate a parameter we denote as the background amplitude residual (BAR) for each ambient measurement cycle for both the 'up' and 'down' ramps to quantify the magnitude of the background changes. A BAR is computed by subtracting the pre- and post-backgrounds point by point over the fit window and then computing the average absolute residual values as voltages, which are then converted to 'relative concentration' units as previously discussed. The BAR values thus calculated provide complementary information to the procedure described by Fried et al. [6] where the pre- and post-backgrounds are fitted, similar to ambient determinations, and the resulting concentrations are subtracted. Figure 9 shows BAR values of 0.16 and 1.32 ppbv, respectively, for specific individual 1-min measurements acquired during the 'stable' and 'perturbed regions' of Fig. 8.

A second diagnostic is to calculate the ambient CH_2O concentrations using only one background at a time rather than the linear time weighted subtraction scheme (LWS). The ambient concentrations thus determined using the pre-backgrounds are designated C_{B1} while those determined using the post-backgrounds are designated C_{B2}, and the resulting concentration differences ($\Delta C = |C_{B1} - C_{B2}|$) provide another indication of when large optical perturbations are present. Figure 12 provides examples of changes in the retrieved concentrations during the 'perturbed region' of July 28 when the two backgrounds were individually employed. In addition to cabin-pressure changes this region was also plagued by perturbations caused by large changes in aircraft speed and pitch, as discussed previously. The third panel down in Fig. 12 displays the resulting 1-s retrievals carried out using the pre- and post-backgrounds for six different 1-min periods. As can be seen, average retrieved concentration differences as large as ~ 1.5 ppbv were observed during one of the periods due to a combination of the perturbations just discussed. In these cases using the pre- and post-backgrounds produced similar ambient concentration time trends only offset from one another. Like the BAR statistic, the calculation of ΔC indicates that a significant change took place between the two backgrounds surrounding each ambient period, but it does not indicate when such change occurred nor whether or not it took place in a smooth linear fashion.

The fitted background absolute area (FBAA) was found to be a useful metric that not only indicated the presence of perturbed spectra, but also when specifically in the 1-min period they occurred. The FBAA was determined by taking the absolute area under the calculated background spectrum determined from the fit parameters A_2 to A_4 in (2) above,
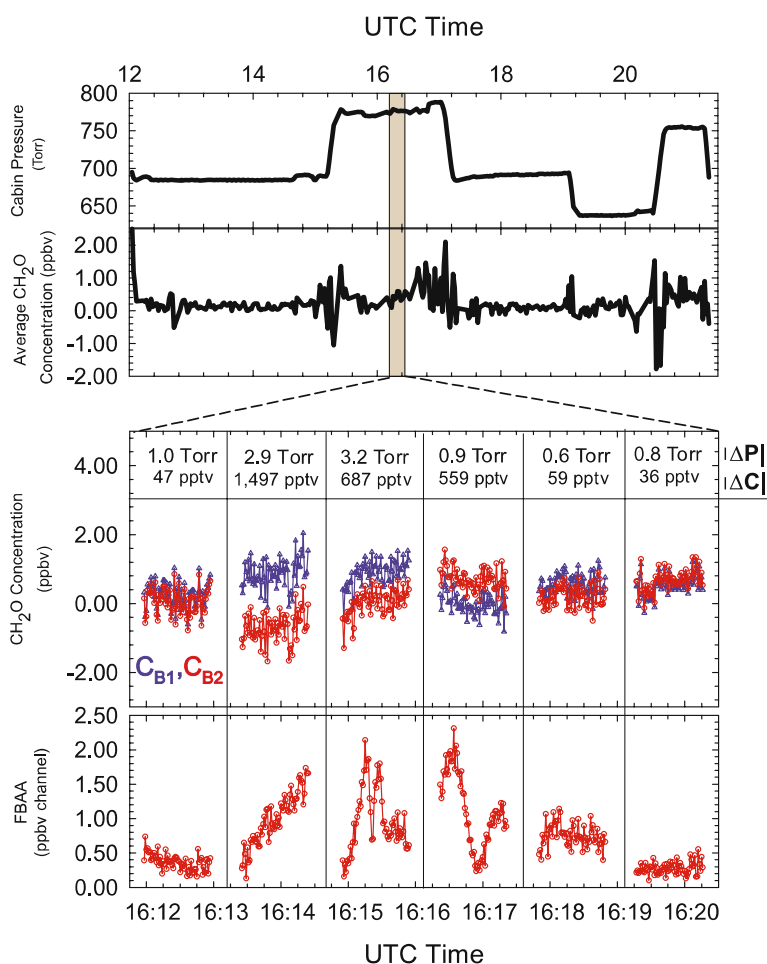
FIGURE 12 (*Upper plots*) Recorded cabin pressures and 1-min averaged CH_2O concentration values for INTEX-NA data collected on July 28th, 2004. The *lower plot* depicts 1-s CH_2O concentration data points for six measurement cycles between 16:12 UTC and 16:21 UTC, where the *blue points* indicate the retrieved CH_2O concentrations when only the pre-background was subtracted (C_{B1}) and the *red concentration points* indicate where only the post-background was subtracted (C_{B2}). The associated change in cabin pressure (ΔP) and a difference in the concentration between the pre- and post-background subtractions (ΔC) is shown. The *lowest plot* depicts the FBAA when the linear time weighted background subtraction scheme is used and indicates when large changes in the background structure of the measured spectra occur. As discussed in the text (Sect. 3.1), the concentration units for the ΔC and FBAA are 'relative concentration' units to be used only as diagnostics and not true measures of measurement precision

yielding a 'relative concentration' area product. As previously indicated, during time periods of perfect background subtraction, these three terms should all be close to zero, which in turn should result in a near-zero calculated background spectrum with a near-zero FBAA value. In the presence of optical perturbations (see lowest panel of Fig. 12) residual background structure in the time period between background acquisitions can change significantly. This will produce non-zero fitted background spectra with large FBAA values and large associated changes for each ambient 1-s data point. Large fitted background areas thus indicate when the LWS is less effective in removing the varying background structure from the absorption spectrum. As can be seen, the three largest ΔC retrievals also produced the largest trends in the FBAA values. In addition, the FBAA in the second block at around 16:14, as an example, shows that the first background is valid while the second background is invalid. A valid second background would have also produced near zero FBAA values at the end of the ambient measurement sequence. The invalid second background is responsible for the linear time trend in the FBAA and the discrepancy in the ΔC values. Most likely optical disturbances affected the acquisition of the second background. By contrast, the third and fourth data blocks at around 16:15 and 16:16 suggest large optical perturbations somewhere near the middle of the ambient acquisitions. Figure 13 shows a much larger portion of the data collected during flight 13 on July 28th than Fig. 12 with the resulting BAR

and FBAA values. These two parameters immediately reveal other optically perturbed time periods throughout this day.

The fit residual (FR), or the square root of the mean-squared error (MSE), can also reveal specific time periods when perturbations are present. These residuals are calculated from

$$FR = \sqrt{MSE}$$
$$= \left(1/N \sum_{i=1}^{N} \left[amb_i - \left(A_1 cal_i + A_2 + A_3 X + A_4 X^2 \right) \right]^2 \right)^{1/2}.$$
$$(4)$$

In principle, the fit residuals should be very useful in immediately identifying specific 1-s perturbed time periods, and indeed in many cases large fit residuals were observed during such time periods. However, there were also many instances where the least-squares fitting routine compensated for large background structural changes by erroneously accommodating such changes in the concentration terms, thus resulting in less dramatic increased fit residuals than one would expect. This occurs when the offset, linear, and quadratic basis vectors cannot accommodate higher-order noise structure. An example of this can be seen in the lowest panel of Fig. 13. Although the largest perturbations evident in the BAR and FBAA diagnostics also appear in the fit residuals (see perturbations at around 20:30), the contrast in the
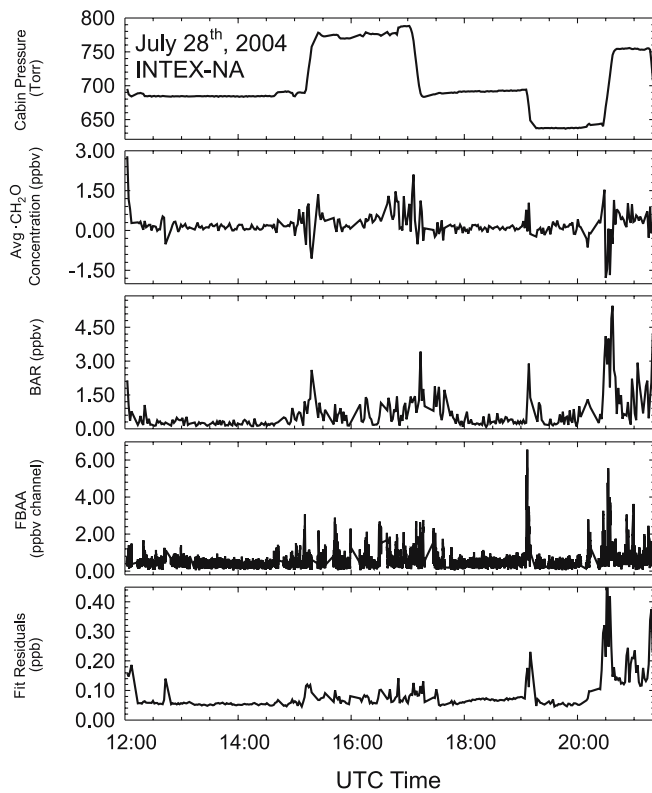
FIGURE 13 Recorded trends of cabin pressure, 1-min averaged CH_2O concentrations, BARs, FBAAs, and fit residuals recorded on July 28th, 2004. As in Fig. 12, the concentration units for the BARs, FBAA, and fit residuals are 'relative concentration' units to be used only as diagnostics and not true measures of measurement precision

fit residuals between 'perturbed' and 'non-perturbed' regions is not as dramatic as the other two diagnostics. In addition, the fit residuals are to some extent dependent upon the ambient concentrations; fitting noise from any number of causes, not just optical perturbations, will thus produce higher fit residual values whenever the ambient concentrations are elevated.

The various measurement parameters described above primarily indicate the stability of the background structure over each background–ambient–background acquisition cycle. By contrast, a new parameter we designate as the average channel standard deviation ($\bar{\sigma}_{ch}$) characterizes the high-frequency noise of the instrument during the acquisition of sample spectra. This parameter, which is calculated using (5), represents the average of the signal standard deviations down each spectral channel in the fitting window across every spectrum collected over the measurement cycle:

$$\bar{\sigma}_{ch} = \frac{\sum_{i=1}^{n} \sigma_i(S_i)}{n}, \tag{5}$$

where

$$\sigma_i(S_i) = \sqrt{\frac{1}{m-1} \sum_{k=1}^{m} \left(S_i(k) - \bar{S}_i\right)^2}. \tag{6}$$

Here σ_i is the standard deviation down the ith channel in the acquired spectra, n is the total number of channels in the fit

window, S_i is an array of spectral data points for the ith channel of length m (where m is the total number of spectral scans for either the 'up' or the 'down' ramp, and has a value of 1500 for 60 s of averaging 25 scans per second), and $\bar{S}_i$ is the mean value. The combined average channel standard is then calculated assuming uncorrelated high-frequency noise between the up and down ramps. Values for $\bar{\sigma}_{ch}$ are then converted from units of volts to relative concentration units as discussed previously.

The $\bar{\sigma}_{ch}$ parameter is very useful in identifying high-frequency noise down each channel and how such noise may evolve between channels over the course of a 1-min measurement. Such noise can arise from fast-moving etalon fringes from aircraft vibrations, rapid fluctuations in cell pressure, air turbulence in the optical train, and intentionally added system vibrations to 'wash out' etalon fringes. Increasing $\bar{\sigma}_{ch}$ values translate to increasing the noise on each 1-s averaged spectrum (i.e. increasing complexity of the background structure on each 1-s spectrum). As a consequence, large $\bar{\sigma}_{ch}$ values will have an effect on fit precision. However, unlike the other parameters just described, $\bar{\sigma}_{ch}$ values are not affected by changing background structure to the same degree from optical perturbations unless the background structural changes occur very rapidly and/or are extremely large in amplitude across most of the channels. Figure 14 illustrates this point. Here we show the PDF distributions for $\bar{\sigma}_{ch}$ and σ_r taken over the stable and perturbed regions for July 28. In contrast to the replicate precision (σ_r), one cannot distinguish the $\bar{\sigma}_{ch}$ distributions between the perturbed and stable regions. It is interesting to note that the $\bar{\sigma}_{ch}$ values are generally lower than the σ_r values, and this most likely reflects the fact that the σ_r values are affected by both background changes and real ambient variability. However, as indicated previously, these two parameters are calculated differently ($\bar{\sigma}_{ch}$ is calculated without fitting an ambient spectrum to a calibration spectrum like the σ_r values). Therefore, the relationship between these two variables is not straightforward. Consequently, we further investigate below the relationship between these two parameters.

Figure 14 shows that the mode for the σ_r distribution (160 pptv) for the stable region is close to that for the $\bar{\sigma}_{ch}$
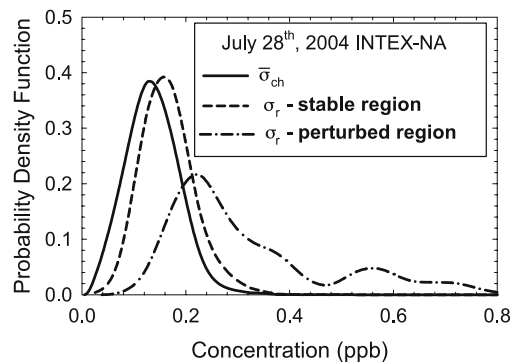

FIGURE 14 Plot of the PDFs for the average channel standard deviation $\bar{\sigma}_{ch}$ (*solid line*) over both the stable and perturbed regions and the replicate precision (σ_r) for the stable measurement period (*dashed line*) and for the perturbed region (*dash-dot line*) depicted in Fig. 8

distribution (130 pptv) and the two curves have very similar Gaussian-like shapes and half widths. Figure 15 shows these results differently by plotting the temporal relationship between these two parameters for both the stable and perturbed regions of July 28th. As can be seen, the replicate precision values during stable time periods approach the $\bar{\sigma}_{ch}$ values and that, with one exception at 15:32 UTC, the $\bar{\sigma}_{ch}$ values are not affected by optical perturbations like the σ_r values. The perturbed region starts around 15:10 and extends past 17:00 (refer to Fig. 8); the large spikes in the σ_r values correlate with those in the retrieved concentration values while the $\bar{\sigma}_{ch}$ values do not show this structure.

Figure 16 shows the relationship between $\bar{\sigma}_{ch}$ and σ_r for all the 1-s measurements averaged over each flight during the entire INTEX study. The reason for the trends in both parameters will be discussed at length in the next section Sect. 3.3. However, the important points to note here are (1) the high degree of correlation between the two parameters (linear regression yields an r^2 value of 0.86) and (2) the significantly lower $\bar{\sigma}_{ch}$ values compared to σ_r, as observed previously in Figs. 14 and 15. At first glance the high degree of correlation between these two parameters seems inconsistent with the behavior shown in Figs. 14 and 15 due to optical perturbations. Figure 16, however, reflects flight-averaged values, which includes both non-perturbed and optically perturbed time periods, and these results imply that additional factors other than slow structural background changes are at work. As discussed previously, increasing $\bar{\sigma}_{ch}$ from increased high-frequency noise gives rise to increased structural changes on every 1-s averaged spectral scan with the consequence that large $\bar{\sigma}_{ch}$ values will have an effect on fit precision. We have observed this behavior in Allan variance plots of the replicate precision with and without additional high-frequency noise using a fan to generate high-frequency vibrations. The high-
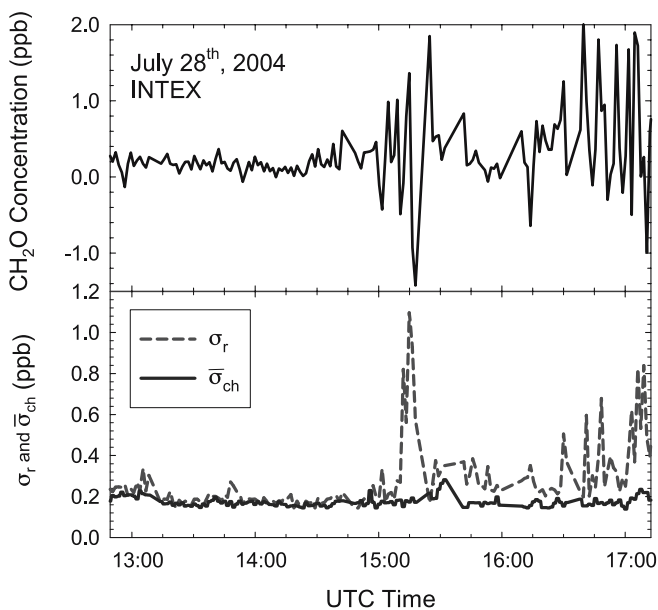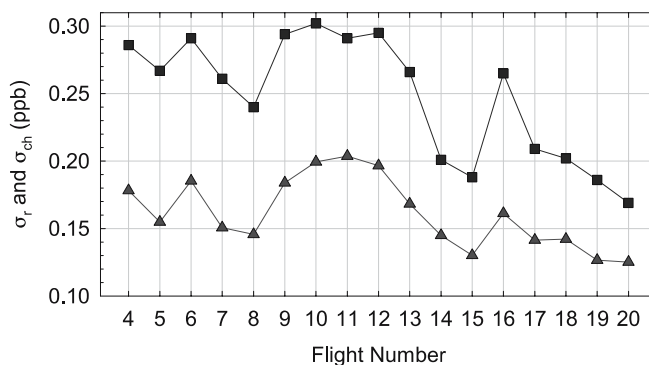

FIGURE 16 Plot of mean average channel standard deviations $\bar{\sigma}_{ch}$ (*triangles*) and replicate precisions σ_r (*squares*) for flight missions 4–20, which exhibit a strong linear correlation to each other of $R^2 = 0.86$. These measurements reflect the average values for all 1-s measurements over each flight

frequency noise degraded the fit precisions by a factor of ~ 3.5 in this one example. Thus, while the $\bar{\sigma}_{ch}$ statistic is not susceptible to slow background structural changes like the σ_r parameter, both are affected by high-frequency optical noise.

The above finding has an important bearing on the strategy one should use in eliminating optical fringes. In the case of large-amplitude, low-frequency fringes, fringe 'washing' by addition of asynchronous vibrations to the optical system should be effective in improving the signal-to-noise up to a certain point. However, since this procedure also adds high-frequency noise to the system, the effectiveness of this approach may be reduced somewhat. In the case of smaller-amplitude and higher-frequency fringes, this approach can actually degrade signal-to-noise unless the added noise is completely random and significantly higher in frequency than the scan time.

3.2 The use of the various diagnostics to identify and eliminate perturbed data

As indicated in the Introduction, one of the objectives of this study was to identify the presence of optical perturbations in flight, allowing for corrective actions to be taken immediately. Where this was not the case, our objective was to identify and eliminate such perturbed data after the fact in our post data analysis using the various diagnostics discussed in the previous section Sect. 3.1. Figure 17 graphically illustrates the mean values and associated standard deviations for each of these parameters for the perturbed and stable time periods of July 28th. As can be seen, the BAR, FBAA, ΔC, and σ_r are dramatically affected by the presence of optical perturbations, which cause large changes in the background structure between background acquisitions. By contrast, the $\bar{\sigma}_{ch}$ and fit residuals are only minimally affected. In recognition of these observations, we employed in our post-processing analysis the BAR, FBAA, ΔC, and σ_r diagnostics in addition to ambient CH_2O concentration trends (presence of large positive and negative concentration swings) and fit background difference values [6] as indicators of when 1-min fit results should be removed from the final data archive. The FBAA values, which have the potential to further indicate the specific individual perturbed 1-s spectra, were not used in this capacity in the present study. Rather than removing the

FIGURE 15 (*Upper plot*) Average 1-min CH_2O concentration time-series data measured on July 28th, 2004 during INTEX-NA. (*Lower plot*) Plot of the replicate precisions, σ_r, and the $\bar{\sigma}_{ch}$ measure. In both cases these precisions refer to the 1-s data over a number of 60-s periods

offending 1-s spectra, the entire 1-min acquisition period was eliminated in the present study.

3.3   *Field improvements to the optical system and acquisition sequence*

Figure 16 shows trends in both $\bar{\sigma}_{ch}$ and σ_r over the course of the INTEX study, and this behavior reflects a number of significant changes to the laser system that have been implemented in the field. It is particularly noteworthy that both $\bar{\sigma}_{ch}$ and σ_r exhibit an increase between flights 8 and 12 and then drop between flights 12 and 13 by approximately the same fractional amount. Between flights 12 and 13 the laser dewar was brought up to room temperature and freshly pumped out. This procedure removes gaseous contaminants that may have deposited inside the dewar between the laser and window, and this significantly reduces laser scattering internal to the dewar and results in an increase in laser power. Of course, the performance improvement may also be associated with other factors like reduced intermode competition noise arising from an improved single-mode output fraction. Whatever the cause, since both $\bar{\sigma}_{ch}$ and σ_r are affected, the additional noise from a dewar that has not been pumped out within ~ 3 weeks appears to have high-frequency components. It is also noteworthy that we implemented a number of other significant improvements to the optical system after flight 13, and this affected both parameters even further, as will now be discussed.

After flight 13 we addressed a number of the optical components responsible for the perturbed performance observed whenever we experienced aircraft cabin-pressure changes and/or accelerations. First, we addressed the multipass absorption cell. As discussed previously, Dyroff et al. [13] observed dynamic flexure of the Herriott cell end plates and base plate as the pressure differential across the cell changes with cabin pressure, causing slight misalignment of the cell mirrors. In addition, as the cell window is sealed using a flexible O-ring, the window moves with changing differential pressure. Both problems cause large changes in background structure. Dyroff et al. [13] were successful in minimizing

the first problem by incorporating four carbon-fiber stabilizing rods on the Herriott cell external structure. Unfortunately, this modification was not possible in the field. A temporary but equally effective solution was implemented in the field by clamping the Herriott cell end plates together with a large commercial pipe clamp. This clamp was positioned and tightened to buck the force exerted by the existing stabilizing rod designed to hold the end plates apart. This effectively reduced changes in the pitch and separation of the cell end plates, and hence cell mirrors, with changing differential pressure. Only slight pressure with the clamp was required to achieve this. Next, we placed an O-ring on the outside of the cell window between the window and the window holder. This O-ring, which was in addition to the sealing O-ring on the cell side of the window, provided enough pressure on the window to minimize window movements with changes in differential pressure across the window. This was accomplished by carefully applying uniform moderate pressure on the window holder after drawing in the window using a vacuum on the cell. The next optical component addressed was the cell input/output mirror mount shown in Fig. 1. Vertical aircraft accelerations produced angular misalignments of the cell input and output beams, which, like the other two optical components, resulted in large changes in acquired background spectra. This problem was addressed using a second clamp to compress the spring in the vertical adjustment arm of the mirror mount. The reference-arm beam splitter shown in Fig. 1 was also locked in place to avoid small refractive displacements in the sample beam with aircraft accelerations. Finally, the $X–Y$ translator mounts on the first OAP shown in Fig. 1 (the OAP closest to the laser dewar) were locked and the micrometers on both stages were disengaged to avoid coupling in forces to the OAP caused by aircraft accelerations.

One final improvement was accomplished by fixing the acquisition of background and ambient spectra to 15 s and 30 s, respectively. Prior to flight 14, background acquisitions were all 10-s long while the ambient periods varied from 30 s to 60 s. This shortened ambient acquisition period reduced the time over which backgrounds were required to be stable, thus helping to ensure that pre-and post-backgrounds more faithfully represented the true background evolution during the ambient acquisition. The lengthened background acquisitions also helped to improve performance by improving the precision of the acquired backgrounds.

Figure 16 shows the dramatic performance improvements achieved using the above solutions starting with flight 14. With the exception of flight 16, both parameters improved dramatically. An inexperienced operator manned the instrument on flight 16 and was unable to optimally align the instrument. Although flight 16 represents an anomaly, it illustrates that even after proper optical stabilization precise optimal alignment is: (1) still an art that is only acquired with flight experience and (2) important for reducing high-frequency noise. Between their peak values experienced during flights 10–12, $\bar{\sigma}_{ch}$ and σ_r both dropped by a factor of ~ 1.4 during the last four flights 17–20, and this improvement was greater than a factor of 1.6 for the last two flights. In addition, after implementing these various improvements we also observed on our oscilloscope display (that displays an average of every two
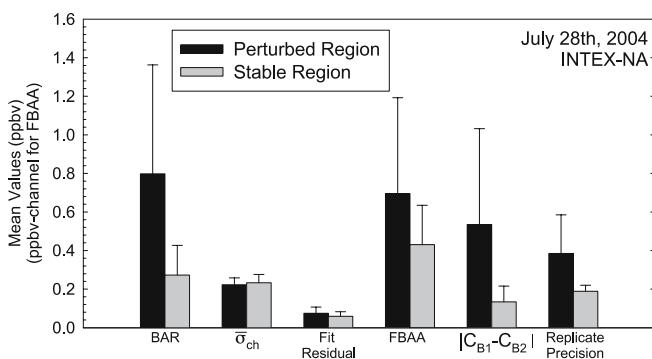

FIGURE 17 Mean and standard deviations of measured statistics taken during July 28th, 2004 for the stable and perturbed regions identified in Fig. 8. This shows the utility of the BARs (ppbv), $\bar{\sigma}_{ch}$ (ppbv), fit residuals (ppbv), FBAA (ppbv-channel), $|C_{B1} - C_{B2}|$ (ppbv), and σ_r in the assessment of measurement perturbation due to background changes. As before, the concentration units for all the parameters except fit precision are 'relative concentration' units to be used only as diagnostics

scans) considerably lower levels of fast-moving optical noise features.

Based on the information just presented, we believe that the various system improvements just described not only improve the stability of the pre- and post-background features (slow noise components) but also reduce high-frequency optical noise features. Furthermore, the σ_r and $\bar{\sigma}_{ch}$ parameters are both affected by such fast optical noise, which apparently is influenced by: (1) the status of the dewar vacuum (build up of gaseous contaminants deposited inside the dewar and/or intermode competition); (2) the opto-mechanical stability of various components; and (3) the specific daily alignment.

The various improvements just described can also be seen by comparing the results of Fig. 18 to Fig. 8 before such improvements were implemented. Figure 18 displays 1-s data for flight 19 acquired on August 13, 2004. Data shown in the cross-hatch-shaded blocks were acquired over time periods with cabin-pressure changes greater than 100 Torr. In contrast to Fig. 8 where cabin-pressure changes of 36 Torr resulted in systematic concentration swings as large as 4.2 ppbv in the retrieved 1-s results, cabin-pressure changes greater than 100 Torr in Fig. 18 induced no such systematic swings. The replicate precisions for the data in the two cross-hatch-shaded blocks ($\Delta P_{cabin} > 100$ Torr) averaged 209 pptv, comparing well with the average value of 177 pptv for the periods shown by the light-gray blocks ($\Delta P_{cabin} < 1.5$ Torr). The slight increase of 18% during pressure changes may be associated with real ambient variability. Nevertheless, the behavior shown in Fig. 18 is significantly improved compared to Fig. 8. This improvement is also shown by the statistics of Fig. 19 compared to Fig. 13 before optics stabilization. The large spikes in the BAR and FBAA statistics present in Fig. 13 are no longer evident in Fig. 19 at equivalent y-axis scales.
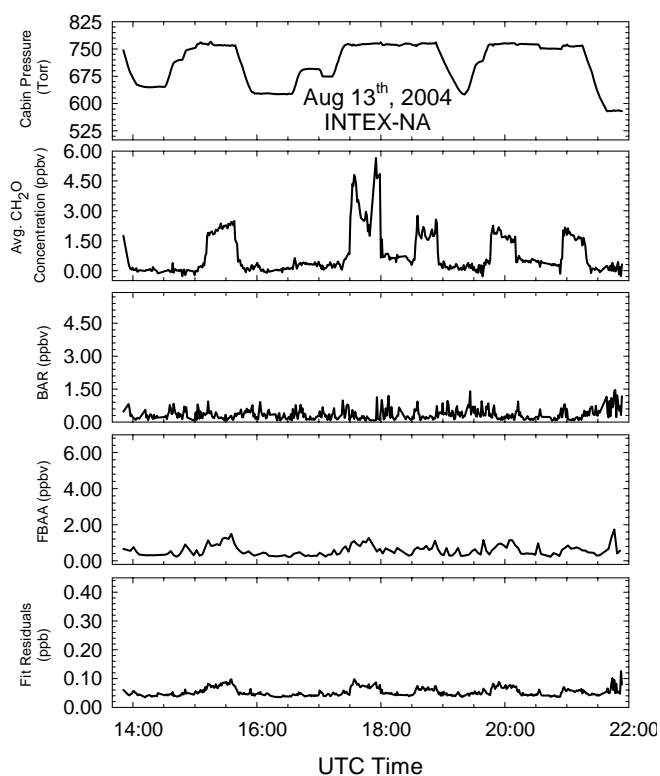

FIGURE 19 Analogous plot as Fig. 13 only for data on August 13th, 2004 after the various optical improvements

Figure 20 shows additional daily flight means for the entire INTEX study. In addition to σ_r and $\bar{\sigma}_{ch}$ mean values, we also plot ΔC and BAR mean values along with their standard deviations. As can be seen, in addition to decreases in the mean values the standard deviations also decrease with the improvements just discussed.
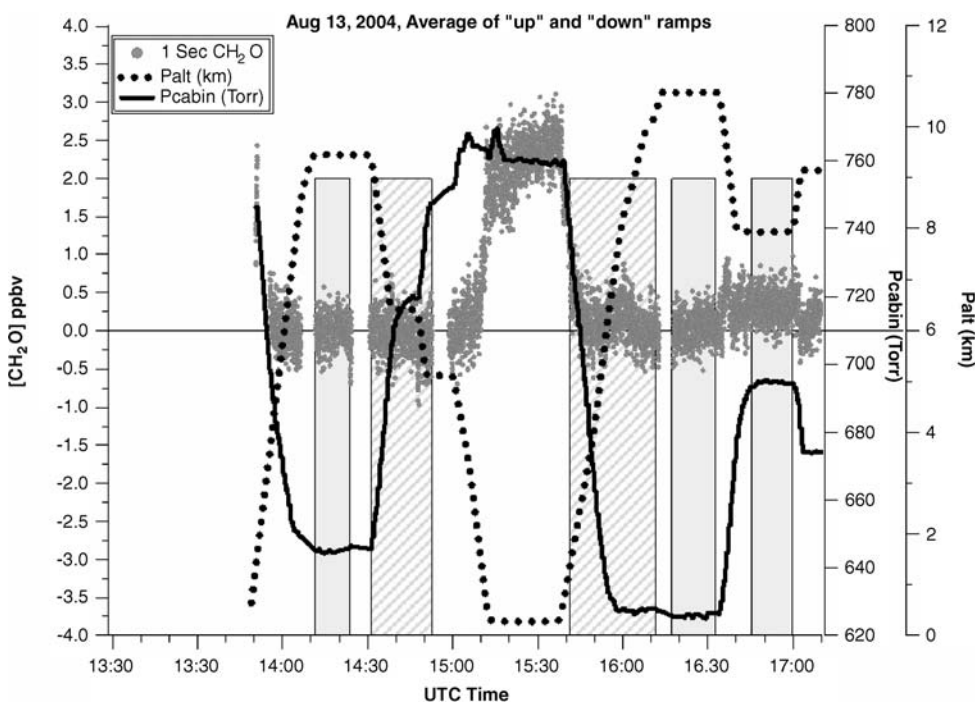

FIGURE 18 Plot of 1-s data for flight 19 acquired on August 13, 2004 after the optical improvements were implemented. Data shown in the *cross-hatch-shaded blocks* were acquired over time periods with large cabin-pressure changes greater than 100 Torr. For comparison purposes, cabin-pressure changes for data in the *light blocks* were all less than 1.5 Torr
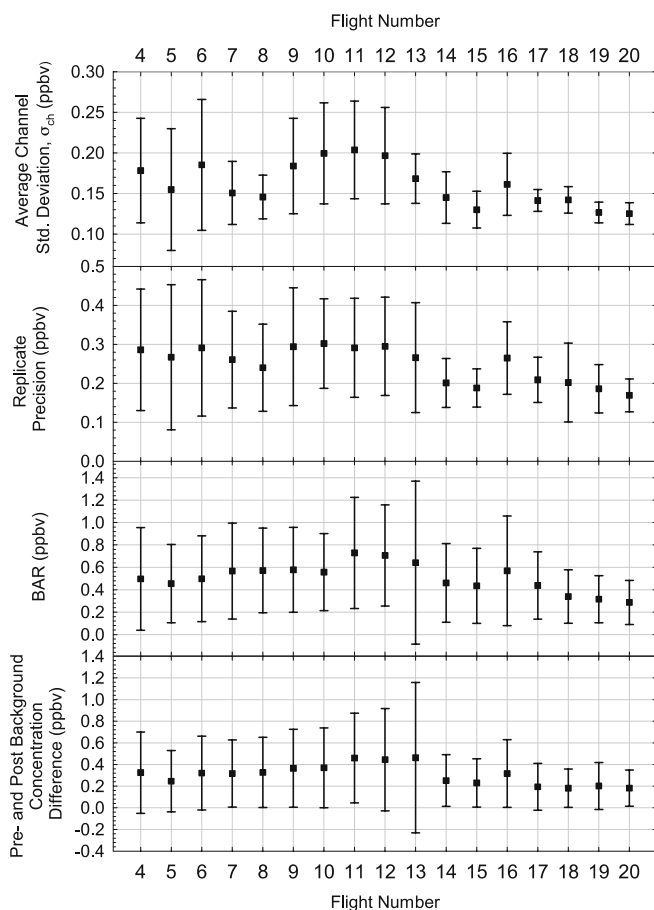
FIGURE 20 Daily means and standard deviations (1σ) for 1-s average channel standard deviations ($\bar{\sigma}_{ch}$), replicate precisions (σ_r), BARs, and $|C_{B1} - C_{B2}|$ taken over 17 of the 18 science flights (flights 4–20) during the INTEX-NA mission. These results are the 1-s flight averages from all the data in each flight and do not refer to specific time periods when we acquire CH_2O time series. As before, the concentration units for all the parameters except fit precision are 'relative concentration' units to be used only as diagnostics

3.4   *The use of replicate precision in estimating* 1-min *limits of detection*

During INTEX the 1-min measurements from various instruments, including the TDLAS described here, were merged into a composite 1-min database. For this purpose it is very useful to provide estimates of 1-min limits of detection (LOD at the 1σ level) from the 1-s data of the present study. Wert et al. [11] discussed the merits of various approaches employed in such estimates during actual airborne operation. As discussed, the replicate precision of 1-min measurements during 'constant air mass periods', periods when ambient CH_2O concentrations are low and stable, may at times be overly pessimistic since true ambient variability can never be ruled out. On the other hand, using stable CH_2O time periods only does not consider true instrument variability due to the types of perturbations discussed in this paper, with the consequence that the LOD may be too optimistic at times. Wert et al. [11] found that the best compromise was to scale the 10-s precision estimates by the square root of the averaging time for all the data. No difference in the results was observed using CH_2O or other ambient tracers to assign 'constant air mass periods'. In this approach the replicate precision of six

10-s measurements, averaged over each 1-min data block, was divided by the square root of 6 and an average value was determined for all the data. This is identical to the replicate precisions (σ_r) of the present study, except that we employ here 1-s measurements.

However, because we have ample evidence that the present instrument, at least during the INTEX-NA study, may only be stable for ~ 30 s to 50 s (see Fig. 2), we conservatively determine a 1-min LOD in all cases by dividing by the square root of 30, even in cases where we acquire 60-s ambient observations. Obviously, a true assessment of instrument stability must come from Allan variance measurements during actual airborne operation. Unfortunately, this comes with the penalty of acquiring background data instead of ambient measurements during costly airborne flights. In addition, a single Allan variance in all likelihood will not represent the Allan variance in all cases (i.e. the Allan variance exhibits a range of values for the optimum stability period), with the consequence that in some cases our assumption of a $\sqrt{30}$ improvement may be too optimistic at times and too pessimistic at other times. However, on average this assumption should be reasonably valid for most cases during INTEX. This has been verified by selecting time periods for replicate 1-min measurements when the ambient CH_2O concentrations were low and stable. In these cases the LOD from σ_r (1-s)$/\sqrt{30}$ was close to that determined from the replicate precision of multiple 1-min measurements. The results of Fig. 2 provide another example where we observe an improvement in precision by $\sqrt{30}$ for measurements carried out at 30 s compared to 1 s.

Aside from the issue of the $\sqrt{30}$ improvement assumption, the 1-min instrument LOD from replicate precision measurements during INTEX will also exhibit a range of values
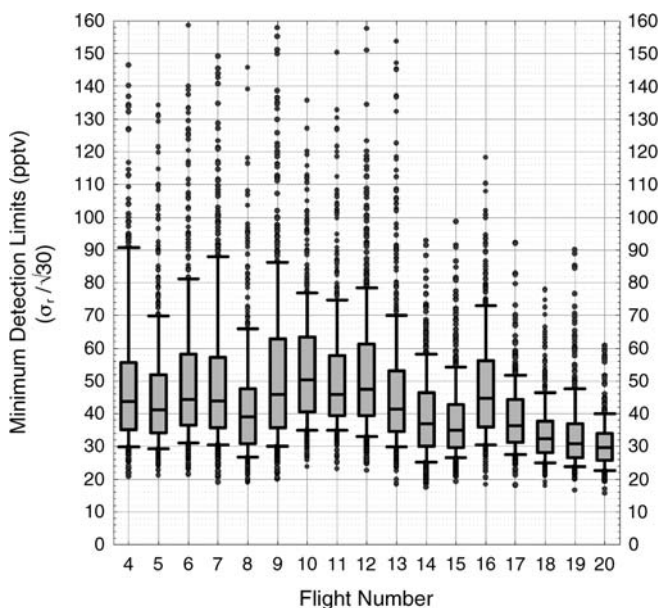

FIGURE 21 Box-whisker chart of scaled replicate precisions ($\sigma_r/\sqrt{30}$) to 30-s integration periods showing the 10th and 25th percentiles, the median, and the 75th and 90th percentiles, which represent the estimated detection limits for flight missions 4–20. Also shown are the outliers below and above the 10th and 90th percentiles. Optical stabilization measures were implemented after flight 13

due to ambient variability. For this purpose we display in Fig. 21 the distribution of the instrument 1-min LOD for every flight (determined by $\sigma_r/\sqrt{30}$). This distribution includes optically perturbed time periods, stable time periods, and time periods when the instrument was not susceptible to aircraft perturbations (flights 14–20), as well as true ambient variability. We display the distributions by box-whisker plots, where the 25th and 75th percentiles are given by the boxes and the median and the 10th and 90th percentiles are given by the horizontal lines. We also display data above and below these outer limits by the points. Even though the distributions for all flights are affected by true ambient variability, the range and median values for flights 14–20 (with the exception of flight 16) after optical stabilization are significantly reduced compared to other flights; the median values are all below 37 pptv and 90% of the values fall within the range of 22 to 58 pptv. For the last three flights (18–20) the median LOD averaged 31 pptv and the 90% range was 22 pptv to 47 pptv (absorbance values in the range between 0.7 and 1.6×10^{-6}). These values are very similar to those reported by Wert et al. [11] for a previous deployment of the present system. The present results of Fig. 21, however, are more robust since they include all the data not pre-selected to eliminate certain time periods. Before stabilization, the median 1-min LOD was as high as 50 pptv and the 90th percentile was as high as 91 pptv with outliers as high as 160 pptv.

4   Summary and conclusions

This paper has addressed a number of improvements to an existing TDLAS instrument for airborne CH_2O measurements during the INTEX-NA mission in the summer of 2004. These improvements involved both data-acquisition software and hardware. Specific improvements included (1) the use of a triangle waveform for scanning the laser to optimize the number of useable spectral channels in the fitting algorithm; (2) the use of larger fitting windows encompassing more background structure; (3) the use of offset, linear, and quadratic background fitting terms; (4) the use of autocorrelation routines for fast data shifting in memory on every scan, for the application of laser wavelength feedback control on slower time scales, and the notification to the instrument operator when new calibration spectra are required; and (5) the implementation of a number of field instrument modifications to eliminate optical perturbations caused by frequent aircraft cabin-pressure changes and accelerations.

In addition, the present paper discussed a number of advanced TDLAS processing concepts to: (1) identify the presence of optical perturbations in flight, allowing for corrective actions to be taken immediately; (2) identify and objectively eliminate such perturbed data after the fact where in-flight corrective actions were not successful; (3) examine the validity of the fitting routines in the presence of such optical perturbations; (4) examine the utility of various diagnostics in helping to elucidate system behavior; and (5) assess the efficacy of various opto-mechanical improvements that have been implemented to the system to minimize such perturbations in the first place.

This paper presented and/or introduced new instrument diagnostics to assess the data quality after the fact, and the comparative utility of each statistic was considered. These diagnostics include the: average channel standard deviation ($\bar{\sigma}_{ch}$), replicate precisions (σ_r), fit residuals, background amplitude residuals (BAR), ambient concentration difference between only pre- and post-background subtractions ($\Delta C = |C_{B1} - C_{B2}|$) retrievals, and fitted background absolute areas (FBAA).

With the exception of σ_r, these statistics are not greatly affected by ambient concentration variability. The replicate precisions are also affected by background changes, whereas the average channel standard deviations are more affected by high-frequency noise, which can have both optical and electronic sources. $\bar{\sigma}_{ch}$ and σ_r were highly correlated. This and other facts presented in this study indicate that in addition to background stability, high-frequency optical noise is also important in dictating overall instrument performance. The BAR, ΔC, and FBAA statistics together with σ_r all revealed the presence of optical perturbations as well as the effectiveness of field instrument modifications to eliminate optical perturbations caused by frequent aircraft cabin-pressure changes and accelerations. Although the various instrument fixes in the field were temporary in nature, they worked exceedingly well to maintain high instrument performance even in the presence of large cabin-pressure changes and aircraft accelerations. The performance of other airborne tunable diode laser absorption spectrometers will undoubtedly benefit from similar improvements.

REFERENCES

1 H. Schiff, G. Mackay, J. Bechera, Air Monit. Spectrosc. Tech. **127**, 239 (1994)
2 D. Brassington, Adv. Spectrosc. **24**, 83 (1995)
3 M. Tacke, F. Wienhold, R. Grisar, H. Fischer, F.-J. Lübken, *Laser Absorption Spectroscopy, Air Monitoring by Tunable Mid-infrared Diode* (Wiley, New York 2000), p. 2033
4 F.K. Tittel, D. Richter, A. Fried, Top. Appl. Phys. **89**, 445 (2003)
5 A. Fried, D. Richter, *Analytical Techniques for Atmospheric Measurement* (Blackwell, Ames, Iowa, 2005) in press
6 A. Fried, B. Henry, B.P. Wert, S. Sewell, J.R. Drummond, Appl. Phys. B **67**, 317 (1998)
7 A. Fried, Y.-N. Lee, G. Frost, B.P. Wert, B. Henry, J.R. Drummond, G. Hübler, T. Jobson, J. Geophys. Res. **107**(D4), 4039 (2002)
8 A. Fried, Y. Wang, C. Cantrell, B.P. Wert, J. Walega, B.A. Ridley, E.L. Atlas, R. Shetter, B. Lefer, M.T. Coffey, J. Hannigan, D. Blake, N. Blake, S. Meinardi, R. Talbot, J. Dibb, E. Scheuer, O. Wingenter, J. Snow, B. Heikes, D. Ehhalt, J. Geophys. Res. **108**(D4), 8365 (2003)
9 A. Fried, J. Crawford, J. Olson, J. Walega, W. Potter, B.P. Wert, C. Jordon, B. Anderson, R. Shetter, B. Lefer, D. Blake, N. Blake, S. Meinardi, B. Heikes, D. O'Sullivan, J. Snow, H. Fuelberg, C.M. Kiley, S. Sandholm, D. Tan, G. Sachse, H. Singh, I. Faloona, C.N. Harward, G.R. Carmichael, J. Geophys. Res. **108**(D20), 8798 (2003)

10 B.P. Wert, M. Trainer, A. Fried, T.B. Ryerson, B. Henry, W. Potter, W.M. Angevine, E. Atlas, S.G. Donnely, F.C. Fehsenfeld, G.J. Frost, P.D. Goldan, A. Hansel, J.S. Holloway, G. Hubler, W.C. Kuster, D.C. Nicks Jr., J.A. Neuman, D.D. Parrish, S. Schauffler, J. Stutz, D.T. Sueper, C. Wiedinmyer, A. Wisthaler, J. Geophys. Res. **108**(D3), 4104 (2003)
11 B.P. Wert, A. Fried, S. Rauenbuehler, J. Walega, B. Henry, J. Geophys. Res. **108**(D12), 4350 (2003)
12 P.O. Wennberg, T.F. Hanisco, L. Jaeglé, D.J. Jacob, E.J. Hintsa, E.J. Lanzendorf, J.G. Anderson, R. Gao, E.R. Keim, S.G. Donnelly, L.A. Negro, D.W. Fahey, S.A. McKeen, R.J. Salawitch, C.R. Webster, R.D. May, R.L. Herman, M.H. Proffitt, J.J. Margitan, E.L. Atlas, S.M. Schauffler, F. Flocke, C.T. McElroy, T.P. Bui, Science **279**, 49 (1998)
13 C. Dyroff, A. Fried, D. Richter, J. Walega, M.S. Zahniser, J.B. Mc-Manus, Herriott cell for trace gas measurements on airborne platforms, in *Conference Proceedings OSA Laser Applications to Chemical and Environmental Analysis (LACEA)*, Annapolis, MD, 2004
14 P. Werle, R. Mucke, F. Slemr, Appl. Phys. B **57**, 131 (1993)
15 A. Fried, J.R. Drummond, B. Henry, J. Fox, Appl. Opt. **30**, 1916 (1991)
16 F.G. Wienhold, T. Zenker, G.W. Harris, Proc. SPIE **2112**, 31 (1994)
17 R.D. May, Rev. Sci. Instrum. **63**(5), 2922 (1992)
18 S.D. Sewell, A. Fried, B.E. Henry, J.R. Drummond, Proc. SPIE **2112**, 72 (1993)
19 B.P. Wert, A. Fried, B. Henry, J.R. Drummond, Proc. SPIE **2834**, 175 (1996)
20 P. Werle, B. Scheumann, J. Schandl, Opt. Eng. **33**, 3093 (1994)
21 W.H. Press, S.A. Teukolsky, W.T. Vetterling, B.P. Flannery, *Numerical Recipes in C* (Cambridge University Press, Cambridge, UK 1992)